EXPERIMENTAL ANALYSIS OF THE EXTENSION TO SHEAR

FRACTURE TRANSITION IN BEREA SANDSTONE

A Thesis

by

JENNIFER KAY BOBICH

Submitted to the Office of Graduate Studies of
Texas A&M University
in partial fulfillment of the requirements for the degree of

MASTER OF SCIENCE

August 2005

Major Subject: Geology

EXPERIMENTAL ANALYSIS OF THE EXTENSION TO SHEAR

FRACTURE TRANSITION IN BEREA SANDSTONE

A Thesis

by

JENNIFER KAY BOBICH

Submitted to the Office of Graduate Studies of
Texas A&M University
in partial fulfillment of the requirements for the degree of

MASTER OF SCIENCE

Approved by:

Chair of Committee,	Fred Chester
Committee Members,	Judith Chester
	Vikram Kinra
Head of Department,	Richard Carlson

August 2005

Major Subject: Geology

ABSTRACT

Experimental Analysis of the Extension to Shear Fracture Transition

in Berea Sandstone. (August 2005)

Jennifer Kay Bobich, B.S., Penn State University

Chair of Advisory Committee: Dr. Fred Chester

To characterize low-pressure, brittle deformation in porous, granular rock, notch-cut cylinders (30 mm neck diameter) of Berea Sandstone were extended in a triaxial apparatus from 10 to 160 MPa confining pressure at strain rates of 10^{-4} s^{-1} and 10^{-5} s^{-1}. Acoustic emission counts were monitored when extending samples at a slow strain rate. Stress at fracture is characterized by the least compressive principal stress, σ_3, and maximum compressive principal stress, σ_1 ($\sigma_1 = Pc$). A change in strength dependence on pressure at $Pc = 50$ MPa corresponds to a change from pure macroscopic extension fracture to mixed-mode opening and shear fracture, and likely reflects the increase in mean stress that suppresses the propagation of extension fractures and the interaction between closely-spaced stepped cracks. Within the extension fracture regime ($Pc < 50$ MPa), σ_3 at failure becomes slightly more tensile with an increase in Pc. At $Pc > 50$ MPa, σ_3 at failure becomes more compressive with an increase in Pc and follows Coulomb behavior; however, the angle between the fracture surface and σ_1 increases continuously with Pc. Fracture surfaces characteristic of the extension to shear fracture transition appear as linked, stepped extension fractures; the length of extensional segments decreases with increasing pressure. The onset of acoustic emissions and

inelastic strain at fracture occurs at earlier points in the strain history with pressure,

consistent with the Griffith prediction of the beginning of fracture growth.

ACKNOWLEDGEMENTS

TABLE OF CONTENTS

LIST OF FIGURES

LIST OF TABLES

INTRODUCTION

An increasing interest in failure of porous, granular rock is a response to recent observations of natural deformation displaying a broad spectrum of failure mode: dilation bands, shear bands, and compaction bands [*Bernard et al.,* 2002; *Mollema and Antonellini*, 1996; *Antonellini et al.*, 1994]. Depending on their dilatant attributes, bands of granular deformation are inherently important to the transport and storage of fluids in the subsurface [*Sibson*, 1996; *Antonellini and Aydin*, 1995; *Antonellini and Aydin*, 1994]; thus the mechanisms required for each mode of deformation need to be understood.

Failure of porous, granular rock exhibits distinctive behavior that follows a nonlinear yield envelope, with positive pressure dependence at low mean stress and negative pressure dependence at high mean stress (Figure 1). The change in pressure dependence of strength generally correlates with the brittle-ductile transition in rock deformation [*Handin et al.,* 1963; *Heard,* 1960]. Detailed experimentation of the negative strength dependence at high mean stress (>200 MPa for Berea Sandstone) documents distributed deformation related to strain hardening and shear-enhanced compaction [*Wong et al.*, 1997; *Zhu et al.*, 1997] and localized deformation in the form of compaction bands [*Challa and Issen*, 2004; *Mollema and Antonellini*, 1996]. Observations of localized granular deformation at moderate and low mean stress (<200 MPa for Berea Sandstone [*Wong et al.*, 1997]) include shear fracture (dilating and

_____

This thesis follows the style of *Journal of Geophysical Research*.
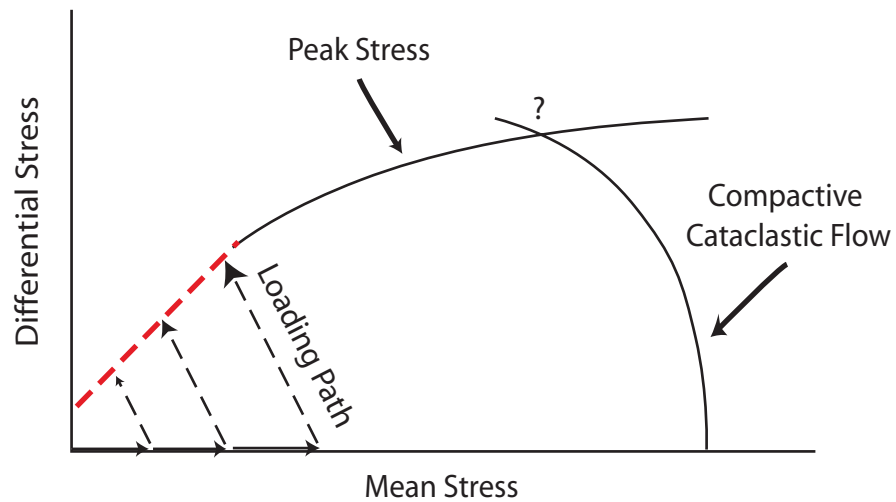
Figure 1. Failure envelope for porous, granular rock. [after *Challa and Issen*, 2004] Extensive experimental studies of compactive cataclastic flow and peak stress have been conducted at high mean stress. This study concentrates on granular deformation at low mean stress, with a loading path depicted with dashed arrows. The results fall within the red, dashed Coulomb portion of the failure envelope, and include loading conditions in which the least principal stress is tensile.

compacting shear bands) [*Besuelle*, 2001; *Besuelle et al*., 2000; *Antonellini et al*., 1994] and extension fracture (dilation bands) that display localized porosity increases as a result of opening-mode displacement [*Issen and Challa*, 2003; *Bernard et al.,* 2002]. In spite of extensive theoretical and experimental work on failure in compressive stress states, relatively little work has investigated failure at mixed tensile and compressive stress conditions.

Experimentation with notch-cut samples in triaxial extension is required to study the extension to shear fracture transition [*Ramsey and Chester*, 2004; *Schock and Louis*, 1982; *Brace*, 1964]. Experimentalists have studied mixed tensile and compressive stress states (condition of hybrid fracture) to compare triaxial extension and compression data [*Brace,* 1964] and to examine strain behavior prior to macroscopic failure [*Schock and Louis,* 1982]. Recent experimentation with Carrara Marble demonstrates a continuous change in fracture orientation and morphology with increasing pressure and a change in strength between extension fracture and hybrid fracture [*Rodriguez*, 2005; *Ramsey and Chester,* 2004]. The degree to which these results apply to granular material is uncertain because of distinct differences in rock microstructure.

In Berea Sandstone, a moderately-cemented sandstone widely studied in rock deformation laboratories [*Wong et al.,* 1997; *Zhu et al*., 1997; *Menendez et al*., 1996; *Hart and Wang,* 1995; *Lockner et al*., 1992; *Bernabe and Brace*, 1990; *Zhang et al.,* 1990], the state of stress in each grain is controlled by grain contacts and macroscopic porosity [*Brzesowsky*, 1995; *Gallagher et al*., 1974]. When a low-pressure differential load is applied to Berea, the dominant deformation mechanisms prior to peak stress are

intergranular microcracking, frictional sliding, and grain-to-grain movement [*Menendez et al.*, 1996; *Bernabe and Brace*, 1990; *Schock and Louis*, 1982]. Proximal to peak stress, intragranular microfracture at Hertzian grain contacts becomes the dominant deformation mechanism [*Menendez et al.*, 1996; *Zhang et al.*, 1990; *Gallagher et al.*, 1974]. Energy released from microcracking, frictional slip, and pore collapse is expressed as acoustic emissions (AE). The deformation prior to macroscopic, brittle failure in Berea Sandstone may be investigated by monitoring AE throughout loading [*Wong et al.*, 1997; *Glaser and Nelson*, 1992; *Lockner et al.*, 1992].

In this study, I investigate brittle failure in Berea Sandstone at low mean stress using triaxial extension of notch-cut cylinders to document behavior of the transition from extension fracture to shear fracture. Inelastic deformation is characterized using mechanical and AE data, and failure surfaces are described in terms of macroscopic orientation and morphology. The failure strengths are used to extend the yield envelope of Berea Sandstone to low mean stress and establish the predictability of fracture orientation. I test the correlation between the pre-peak-stress surge in acoustic emissions due to intergranular cracking and frictional sliding, known as the point of shear-induced dilation in the brittle regime [*Wong et al.*, 1997], and the onset of inelastic strain between extension and shear fracture. Accordingly, the capability of the Griffith theory to predict initiation of fracture development, as defined by acoustic emission activity and failure data, is determined. All results are compared to failure characteristics of low-porosity, polycrystalline calcite Carrara Marble, deformed under similar experimental conditions [*Ramsey and Chester*, 2004].

METHOD

Sample Description

Berea Sandstone, taken from Cleveland Rock Quarries in Ohio, has been widely studied in rock deformation laboratories worldwide due to the homogeneity in grain size and mechanical behavior of samples. Attributes of the undeformed sandstone in this study (Table 1) are comparable to previous measurements [*Menendez et al.,* 1996; *Hart and Wang,* 1995; *Bernabe and Brace,* 1990; *Zhang et al.,* 1990]. A porosity of 19% was determined from saturating the rock with alcohol and calculating the mass difference between a volume with the bulk rock density and a volume with the density of alcohol. The Schwartz-Saltykov method [*Hillard and Lawson*, 2003] was used to determine the grain size distribution from measurements of grain diameter in plane petrographic sections; the mean diameter is 185 μm. The subangular, well-sorted grains include 75 to 80% quartz and 20 to 25% feldspar, dolomite, rutile, zircon, kaolinite, and some secondary minerals [*Hart and Wang,* 1995; *Bernabe and Brace,* 1990; *Zhang et al.,* 1990]. Dolomite grains and cement (up to 400 μm) are distributed throughout the granular mass. Berea exhibits numerous visible laminae defined by mafic minerals on the order of 0.5 mm spacing that may influence fracture initiation and propagation. Accordingly, 5-cm-diameter cores are taken parallel (within 6°) to the laminae to mimic an Andersonian geologic setting with the least principal stress parallel to laminae.

TABLE 1. Rock Properties of Berea Sandstone and Carrara Marble

Rock Type	Composition	Compressive Strength (MPa)	Tensile Strength (MPa)	Mean Grain Size (μm)	Porosity (%)
Berea Sandstone	[1] 75-80% quartz 20-25% feldspar, dolomite, rutile, zircon, and kaolinite	[2] 79	4.9 - 7.3	185	19
Carrara Marble	[3] ~98% calcite	[4] 92	[3] 7.5	[3] 250	[3] < 1

[1] [*Hart and Wang,* 1995; *Bernabe and Brace,* 1990; *Zhang et al.,* 1990]

[2] [*Teufel and Clark*, 1984; *Krech et al.*, 1974]

[3] [*Ramsey and Chester*, 2004]

[4] [*Cruden*, 1971]

Using a microlathe on a stationary surface grinder, the cores are ground to a notch-cut, or 'dog bone,' geometry [*Ramsey and Chester*, 2004; *Mardon et al.*, 1990; *Johnson et al.*, 1987; *Schock and Louis*, 1982; *Brace*, 1964] that is ideal for controlled fracture during extension experiments. The novelties of the notch-cut geometry are that the fracture always forms at the single stress concentration in the center of the neck, the stress is fairly uniform in the neck, and end effects are obviated, enhancing reproducibility of experiments. In addition, the difference in area between the shoulders and neck allows for axial tensile stress to develop in the neck during extension (Figure 2). The samples are 102 ± 4 mm in length, with a large (shoulder) diameter of 46.9 ± 0.1 mm and small (neck) diameter of 30.33 ± 0.03 mm. The neck of the samples has a radius of curvature of 87.6 ± 1.3 mm.

A single polyolefin outer jacket is affixed to the piston/sample assembly with nicrome tie wires to prevent intrusion of the confining fluid. The polyolefin supports relatively large elastic stresses and results in undesirable loading if in direct contact with the sample notch. Accordingly, a layered inner jacket is employed, following the design of *Ramsey and Chester* [2004]. Plasticene modeling clay is molded around the sample neck and flush with the shoulders to evenly distribute the confining pressure over the entire notch and to prevent the outer polyolefin layer from contacting the neck (Figure 3). The clay needs to be restricted from intruding into fractures and pores, so innermost jackets are used of either latex (0.2 mm thick) to attain strength data, or copper (0.06 mm thick) to preserve the fracture surface from post-fracture clay intrusion.
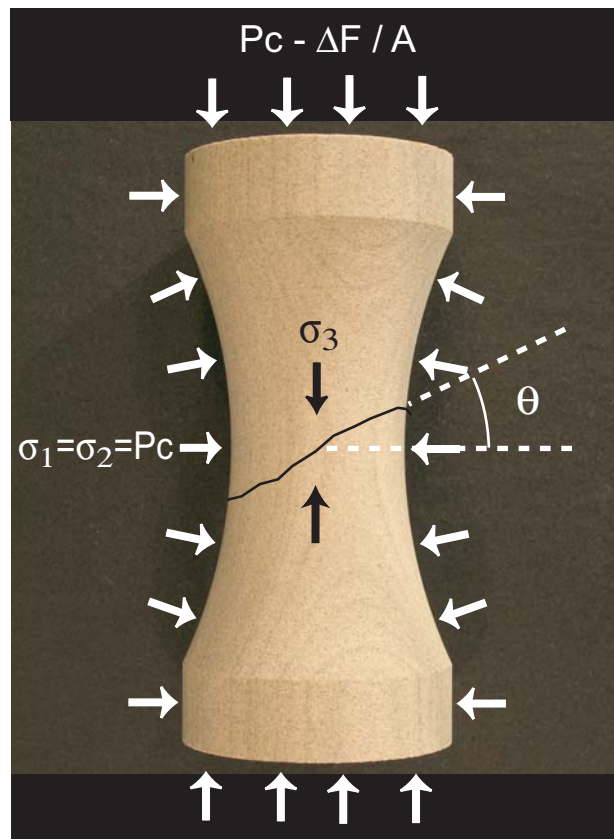
Figure 2. Stress conditions on the sample. Fracture angle θ is the maximum angle between the best-fitting plane through the fracture surface and the plane perpendicular to the cylinder axis.
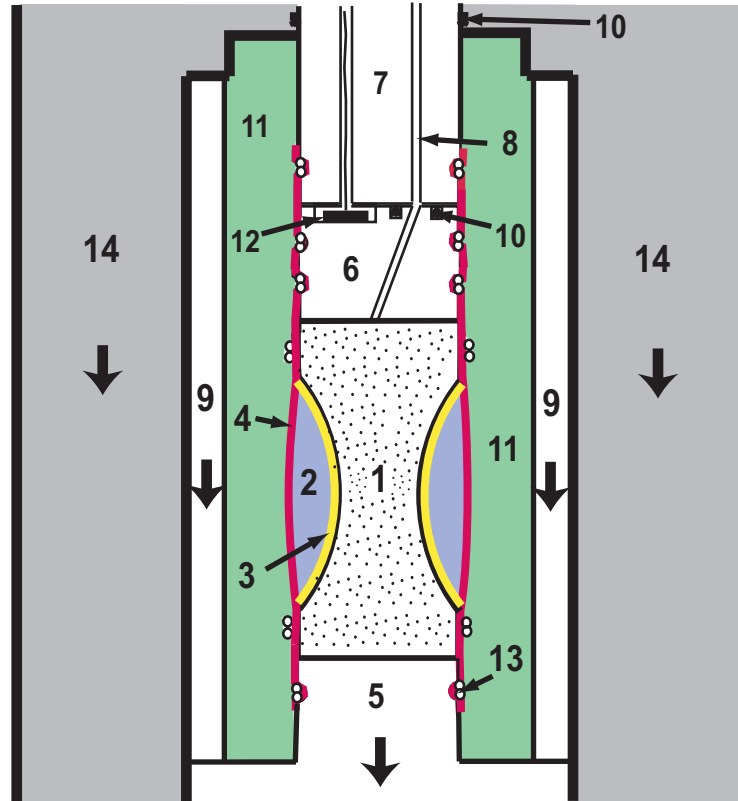
Figure 3. The sample assembly in the Large Specimen Rig. Numbers indicate the following: sample (1), clay (2), copper or latex inner jacket (3), polyolefin outer jacket (4), lower piston (5), end cap (6), upper piston (7), pore pressure vent (8), steel ring (9), o-ring (10), confining fluid (11), piezoelectric transducer (12), tie wires (13), and thick-walled pressure vessel (14). The pressure vessel, steel ring, and lower piston move down with respect to the upper piston in extension experiments.

Experimental Apparatus and Procedure

The jacketed samples are deformed in the Large Specimen Rig (LSR) of the John Handin Rock Deformation Laboratory, a liquid-confining media, gear-driven triaxial apparatus equipped for measurement of acoustic emissions (AE). Axial force, axial displacement, and confining pressure (Pc) are recorded with accuracy of ±1026 N, ±0.005 mm, and ±0.3 MPa, respectively. Latex- and copper- jacketed samples are extended at 10 to 160 MPa confining pressure, room temperature (22 ºC) and humidity, and axial displacement rates of 0.02 mm s^{-1} (no AE recorded) and 0.001 mm s^{-1} (AE recorded). The experimental procedure involves establishing confining pressure and extending the piston for 8 mm prior to loading the sample in order to establish a reference for measuring differential force independent of o-ring friction. The extension of the piston is stopped as soon as a macroscopic stress drop associated with fracture occurs, and then Pc is reduced. Although this unloading path was chosen to minimize additional damage to the fracture surface, acoustic emissions likely associated with formation of secondary 'unloading' fractures occur. Reproducibility experiments at confining pressures of 10 and 120 MPa with latex jackets and 100 MPa with copper jackets indicate reproducibility errors of ±0.5 MPa for latex-jacketed samples, and ±1 MPa for copper-jacketed samples. These likely reflect variability in both sample and jacket strength as well as measurement accuracy.

To record acoustic emissions (AE), the upper piston accommodates the use of a Lead Zirconate Titanate piezoelectric transducer, podded into a steel end cap 33 mm from the end of the sample with insulating epoxy (Figure 3). Silicone gel is applied to

the ends of samples to enhance transmission of acoustic signals across the sample-end

cap interface (Figure 3). Experiments that record acoustic emissions are run at a lower

axial displacement rate of 0.001 mm s^{-1} to facilitate counting individual events. The

signals from typical AE events are up to 400 µV amplitude and 1ms duration. Amplified

and filtered signals (Figure 4) range between 150 mV and 1.2 V in amplitude for all

experiments. A comparator is set to count events above 130 mV amplitude. When

events are so frequent as to saturate the integrator, the monostable multivibrator counts

every 1.9 ms, resulting in AE rates of 500 counts/sec. Very few false counts are due to

noise, and approximately 3% of total counts are a result of large events being falsely

counted multiple times. AE count rates are filtered with a moving average over 10 data

points (7 sec).

Observation of Deformed Samples

Samples jacketed with copper are used for inspection of fracture surface

morphology and to determine fracture orientation. Latex-jacketed samples are intruded

by clay after fracture formation, thus fracture surfaces are cleaned with hot soapy water

prior to orientation measurements. Macroscopic orientation of fracture surfaces is

determined by point-sampling one side of each fracture surface with a drag profilometer.

A 24-point grid is used, with data points spaced 5 mm apart and orientation constant

between samples. The orientation of a best-fit plane is determined using a multiple

linear regression of the measured points, which establishes the fracture orientation with

respect to the sample axis (Figure 2) and to the sandstone block frame of reference.

Fracture surfaces from copper-jacketed experiments are photographed, and the resulting

images are thresholded to the point where laminae are just indistinguishable in order to
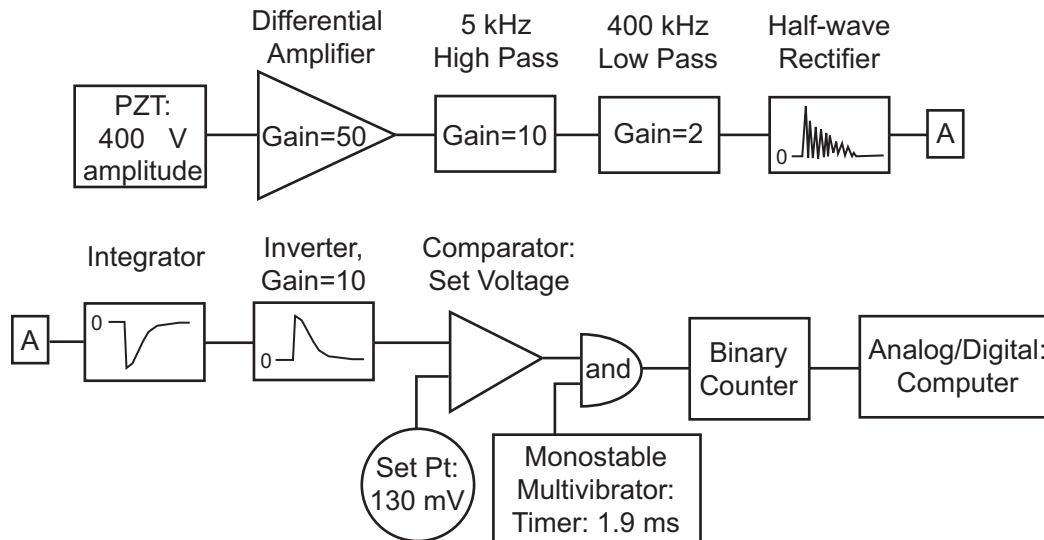
highlight fracture surface features.

Figure 4. Block diagram of the acoustic emission acquisition system. Raw signals of 400 µV amplitude are amplified to 1.2 V, filtered, rectified and integrated. The comparator is set to count events above 130 mV amplitude. When multiple, closely timed AE events saturate the integrator, the monostable multivibrator counts every 1.9 ms.

TABLE 2. Experimental results, not corrected for jacket type

Experiment	$\sigma_1 = Pc$ (MPa)	σ_3 (MPa)	Fracture Angle (°)	σ_n (MPa)	[3] Total AE (count)	Audible Fracture	Inelastic Strain (%)
[1] *Latex Jacket, 0.02 mm/s*							
[2] 4784	10.1	-4.9	3.1	-4.9	-	no	-
4795	10.1	-5.6	6.7	-5.3	-	yes	-
4779	20.1	-6.2	3.5	-6.1	-	yes	-
4782	30.2	-6.6	2.6	-6.5	-	yes	-
4777	40.0	-7.0	-	-	-	yes	-
4780	50.2	-7.3	2.5	-7.2	-	yes	-
4778	60.3	-5.9	6.2	-5.2	-	no	-
4802	70.7	-5.5	3.5	-5.2	-	no	-
4774	80.3	-2.3	6.1	-1.3	-	yes	-
4805	90.4	-1.4	2.7	-1.2	-	no?	-
4775	100.5	0.9	7.9	2.8	-	yes	-
4806	110.5	1.7	-	-	-	yes	-
4776	120.6	4.5	9.8	7.9	-	yes	-
4809	120.5	3.7	11.4	8.3	-	yes	-
4807	130.7	3.9	4.3	4.6	-	yes	-
4781	140.5	5.8	10.7	10.4	-	yes	-
4808	150.7	8.0	13.4	15.6	-	yes	-
4783	160.8	10.3	13.4	18.4	-	yes	-
Copper Jacket, 0.02 mm/s							
4794	20.1	-6.9	1.9	-6.8	-	yes	-
4796	40.2	-7.9	1.4	-7.9	-	yes	-
4793	60.4	-6.8	3.0	-6.6	-	no	-
4791	80.4	-3.5	6.5	-2.5	-	yes	-
4790	100.5	-2.1	6.5	-0.8	-	yes	-
4797	100.5	-1.1	5.3	-0.2	-	yes	-
4798	120.5	0.8	9.7	4.2	-	yes	-
4792	140.8	5.9	15.4	15.4	-	yes	-
4813	160.8	7.5	14.2	16.7	-	yes	-
Copper Jacket, 0.001 mm/s							
4832	10.0	-6.0	3.8	-5.9	171	yes	0.0
4834	30.2	-6.9	1.3	-6.9	228	yes	0.0
4835	50.0	-6.9	3.0	-6.8	926	yes	0.0
4827	70.2	-4.6	6.5	-3.7	1368	no	2.0
4824	90.3	-2.4	3.1	-2.1	2563	no	13.2
4831	110.0	2.2	12.7	7.5	5658	yes	33.3
4821	130.9	4.3	12.2	9.9	5057	yes	32.2

[1] Displacement rate

[2] Two fractures at fracture formation

[3] At stress drop; includes hit point AE in experiments 4832 and 4827

RESULTS

Successful experiments consist of 18 latex-jacketed samples and 9 copper-jacketed samples without recording AE, and 7 copper-jacketed samples with AE recorded (Table 2). The latex-jacketed samples provide accurate mechanical data, and the copper-jacketed samples are used to analyze fracture characteristics, such as orientation and surface morphology.

Mechanical Data

Stress-strain curves for latex and copper experiments are similar in appearance, except for small systematic differences in strength as a result of the copper. The curves exhibit elastic behavior prior to inelastic yielding, followed by a stress drop that coincides with formation of a macroscopic fracture. Young's modulus of Berea appears to increase with pressure, from 8 GPa at the lowest confining pressure to 24 GPa at a pressure of 160 MPa, although this may be due in part to stiffening of the experimental column with pressure. At Pc < 50 MPa, fracture occurs after minimal inelastic deformation. At Pc > 50 MPa, fractures form after nonlinear inelastic yielding and a plateaued peak stress. The reproducibility of stress-strain response is good on the basis of systematic variations with Pc and results of duplicate experiments (Figure 5).

Acoustic emissions were monitored throughout seven experiments conducted at an axial displacement rate of 0.001 mm s^{-1} (Table 2). Generally, acoustic emission rate increases monotonically between the hit point and the beginning of stress drop. Cumulative acoustic emissions at fracture formation increase with pressure from 26 (Pc = 10 MPa) to 5060 (Pc = 130 MPa) counts (Figure 6). For all experiments, it is difficult
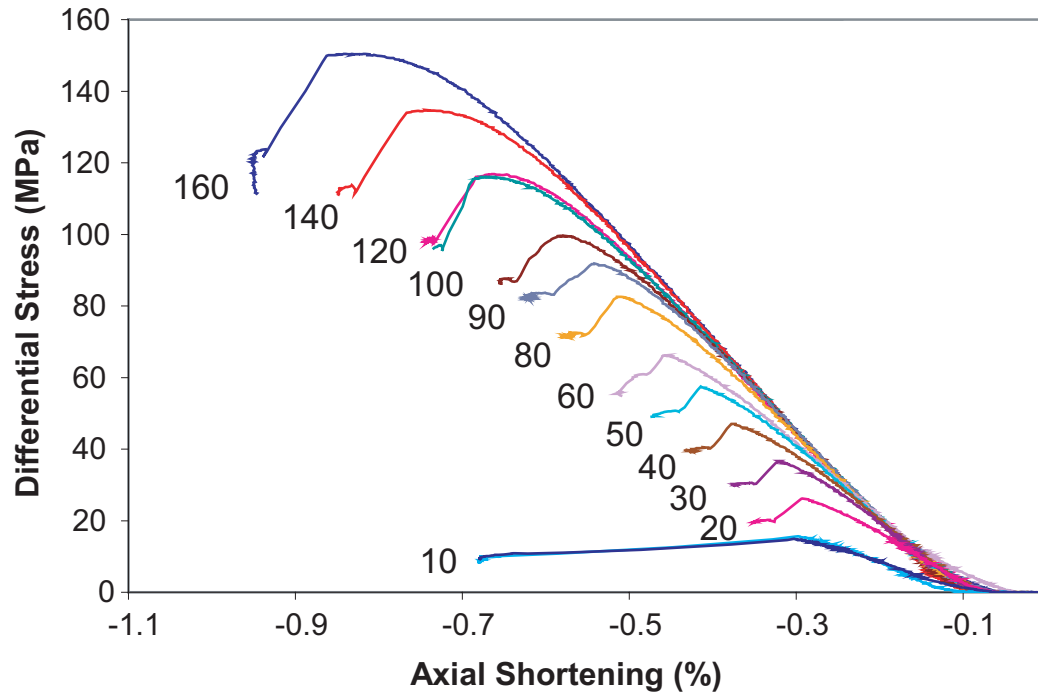
Figure 5. Failure curves for Berea Sandstone in extension. The maximum principal stress is indicated next to respective curves, with reproducibility of curves at 10 and 120 MPa. Pc < 100 MPa: mixed compressive and tensile stress states, Pc > 100 MPa: compressive stress states
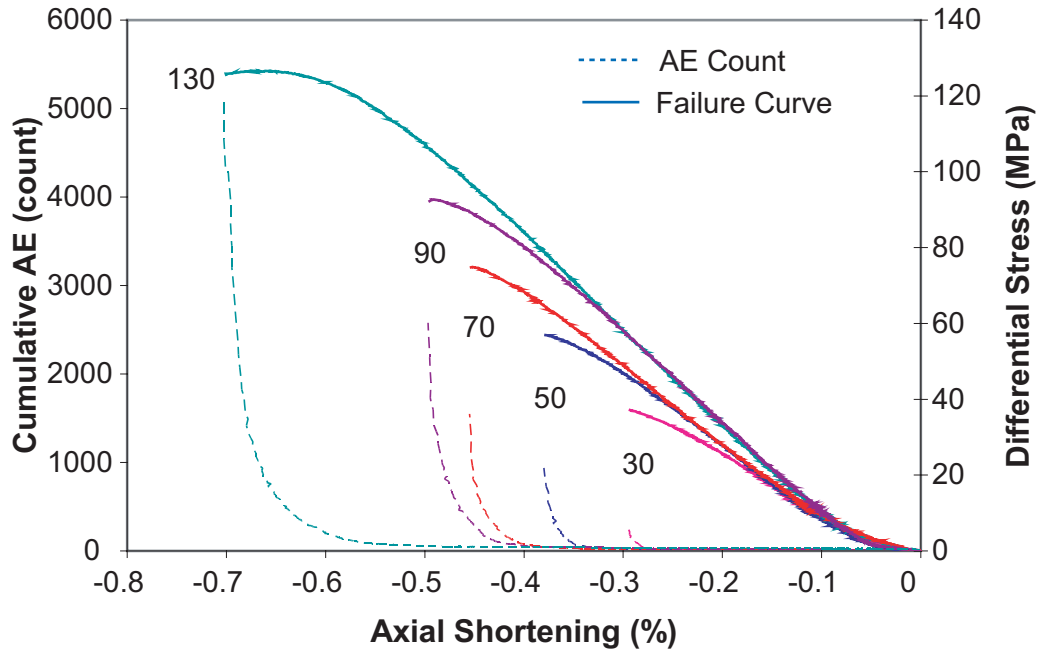
Figure 6. Failure curve and cumulative acoustic emission count comparison. The data are from the hit point to the stress drop of copper-jacketed experiments run at a strain rate of 10^{-5} s^{-1}. The maximum principal stress is indicated next to respective curves.

to distinguish the initiation of AE due to the very gradual increase in events as differential load is increased.

Latex-jacketed samples are assumed to exhibit the true strength of the material because the latex is very weak [*Ramsey and Chester*, 2004]. Therefore, the difference in strength between the copper- and latex- jacketed samples is used to determine the strength of the copper jacket for correction of fracture strength determinations. The strength difference between copper and latex experiments at the same displacement rate of 0.02 mm s^{-1} increases with Pc (Figure A-1). In contrast, latex experiments run at a displacement rate of 0.02 mm s^{-1} and copper-jacketed samples at 0.001 mm s^{-1} show a fairly consistent difference in strength of approximately 0.5 MPa at the same Pc. In this case, the similarity in strength could reflect competing dependence of the jacket and rock. These two data sets are fit by the linear relation,

$$\Delta\sigma_{jacket} = a + bPc \qquad\qquad (1).$$

At an axial displacement rate of 0.02 mm s^{-1}, $a = 0.56$ MPa and $b = 0.012$, whereas at the axial displacement rate of 0.001 mm s^{-1}, $a = 0.47$ MPa and $b = 0.001$. The relationship in (1) is used to remove jacket strength and rate effects in determination of fracture strength of copper-jacketed samples.

Fracture strength is taken as the greatest differential stress achieved in stress-strain curves (Figure 5, Table 2), and is characterized in σ_3 versus σ_1 (=Pc) plots (Figure 7). At confining pressures less than 50 MPa, σ_3 decreases (becomes more tensile) from -4.9 MPa to -7.3 MPa with increase in Pc from 10 to 50 MPa, respectively. A change in the dependence of σ_3 on Pc occurs at a confining pressure of 50 MPa, above which
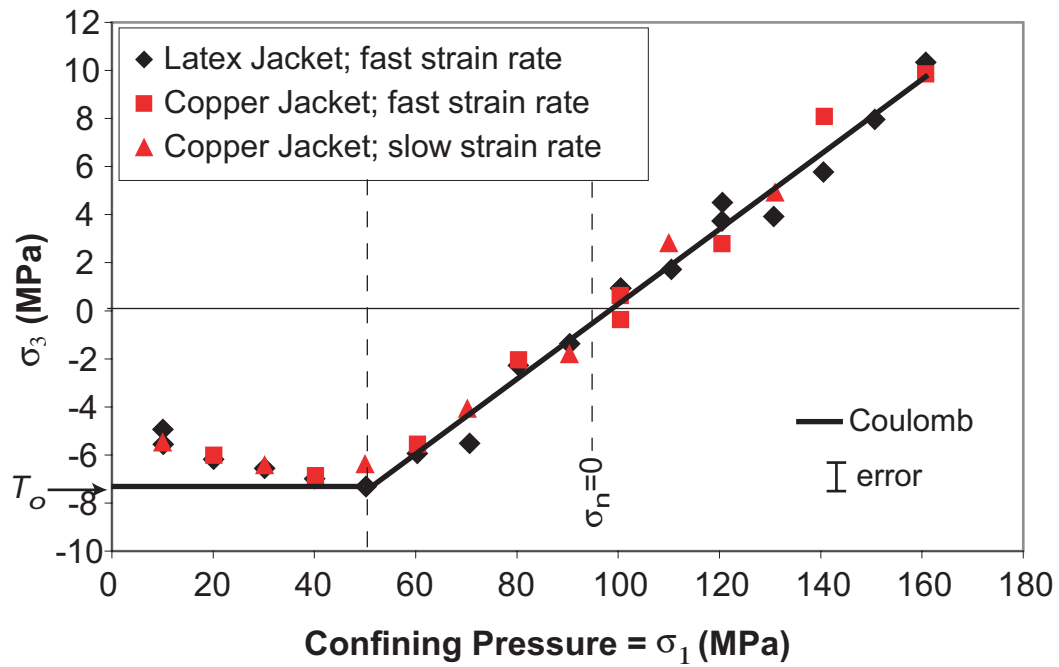
Figure 7. Maximum and minimum principal stress at peak stress. Failure data from Berea Sandstone samples jacketed in copper have been corrected with respect to data from latex-jacketed samples. The error bar represents experimental error. The black line is the Coulomb failure envelope. The dashed line at Pc = 95 MPa defines zero normal stress across the fracture surface. Slow strain rate = 10^{-5} s^{-1}, fast strain rate = 10^{-4} s^{-1}

σ_3 increases (becomes more compressive) with an increase in Pc (Figure 7). At $Pc > 50$ MPa, σ_3 increases linearly and is well fit ($R^2 = 0.983$) by the Coulomb relationship

$$\sigma_1 = a + b\,\sigma_3 \qquad\qquad (2),$$

where $a = 98.7$ MPa and $b = 6.4$.

Audible fracture formation occurs at both slow and fast strain rates and with both jacket types. Fracture formation was not audible in 7 experiments (Table 2), 6 of which formed under mixed stress states (compressive σ_1 and tensile σ_3).

The amount of inelastic strain prior to fracture formation is measured by comparing stress-strain behavior to a nonlinear elastic reference. The elastic reference is defined by stacking axial stress versus axial strain curves such that the elastic portions coincide and may be described by a single, nonlinear curve (Figure 8). The difference between strain at failure and the elastic reference at the same axial stress defines the inelastic strain prior to fracture formation (Table 2).

Fracture Characteristics

The maximum angle between the best-fit plane to the fracture surface and the plane normal to the sample axis (σ_1-σ_2 plane) is defined as the fracture angle. Fracture angle increases from 2° to 15° with pressure (Figure 9, Table 2), independent of jacket type and strain rate. Fracture angles formed at $Pc < 60$ MPa are $\leq 4°$, independent of pressure. At $Pc > 60$ MPa, fracture angles increase monotonically with pressure, to 15° at $Pc = 160$ MPa.
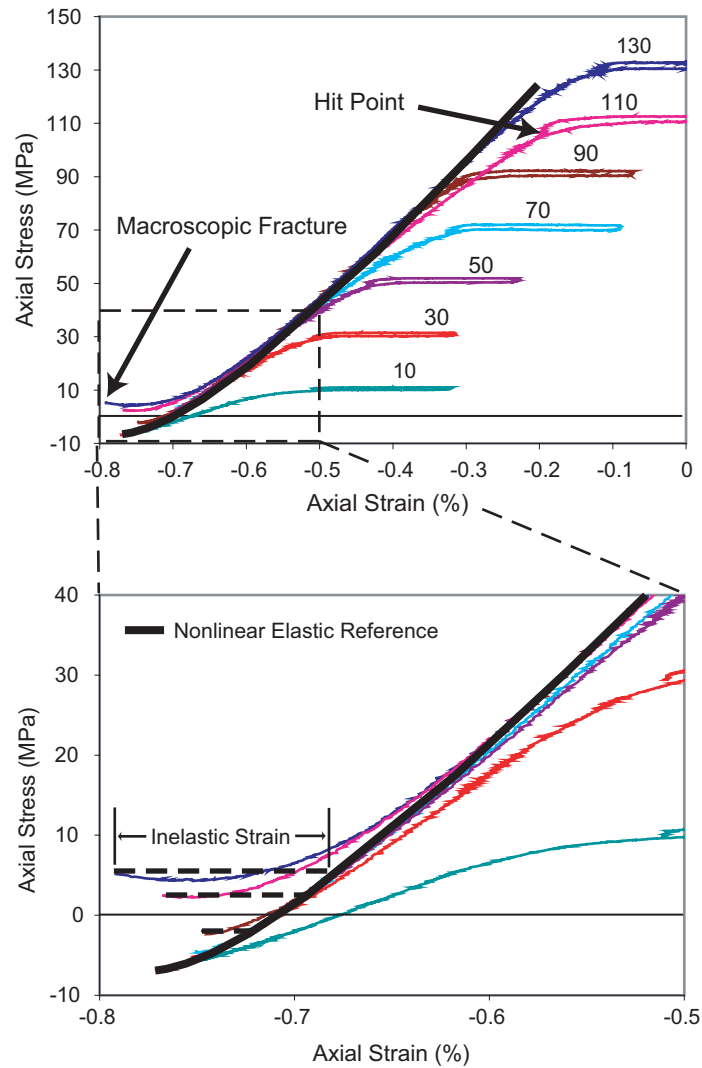
Figure 8. Method of determining the amount of inelastic strain prior to macroscopic fracture. The axial stress versus axial strain curves are from copper-jacketed experiments run at a strain rate of 10^{-5}. *Upper:* The nonlinear elastic reference curve (dark black line) is fit to the aligned, elastic portion of the failure curves. Confining pressures (MPa) are shown next to respective curves. *Lower:* A detailed view of the inelastic portion of the failure curves shows the difference in strain (dashed black line) measured between failure and the elastic reference at the same axial stress.
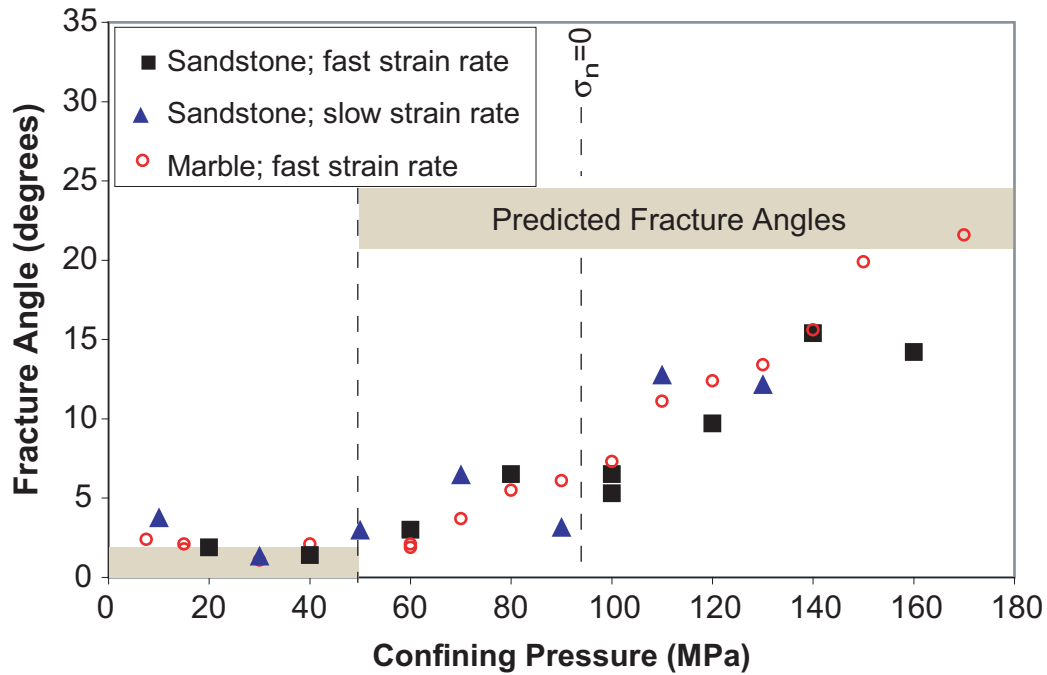
Figure 9. Change in fracture angle with pressure. Data are from copper-jacketed samples of Berea Sandstone and Carrara Marble [*Ramsey and Chester*, 2004]. Although not shown, fracture orientations of latex-jacketed samples fall along the trend set by copper-jacketed samples. Shaded areas are predicted angles from a Coulomb analysis of strength data from samples jacketed with latex. The range of predicted fracture angles indicates the error of possible points of tangency to Mohr circles. Slow strain rate = 10^{-5} s^{-1}, fast strain rate = 10^{-4} s^{-1}

The *Pc* where the normal stress (σ_n) on the fracture surface changes from tensile to compressive is *Pc* = 95 MPa, which is determined through transformation of principal stresses and the observed fracture angle (θ) using

$$\sigma_n = \frac{\sigma_1 + \sigma_3}{2} - \frac{\sigma_1 - \sigma_3}{2} * \cos(2\theta) \qquad (3).$$

Fractures are macroscopically planar, with surface morphologies that are either granular and tan or comminuted and white, or a combination of the former. The white, comminuted zones are part of the surface because they remain after the sample has been washed with hot soapy water. Moreover, the location of the white patches can be matched on both faces of the fracture.

At *Pc* < 50 MPa, only granular, tan fracture surfaces are produced. At 50 MPa < *Pc* < 160 MPa, zones of white comminution coexist with the granular, tan morphology. The spacing of comminuted zones decreases with pressure (Figure 10). At *Pc* = 160 MPa, the entire surface is white and comminuted. The amount of comminution on fracture surfaces formed at different strain rates is comparable (Figure 10).
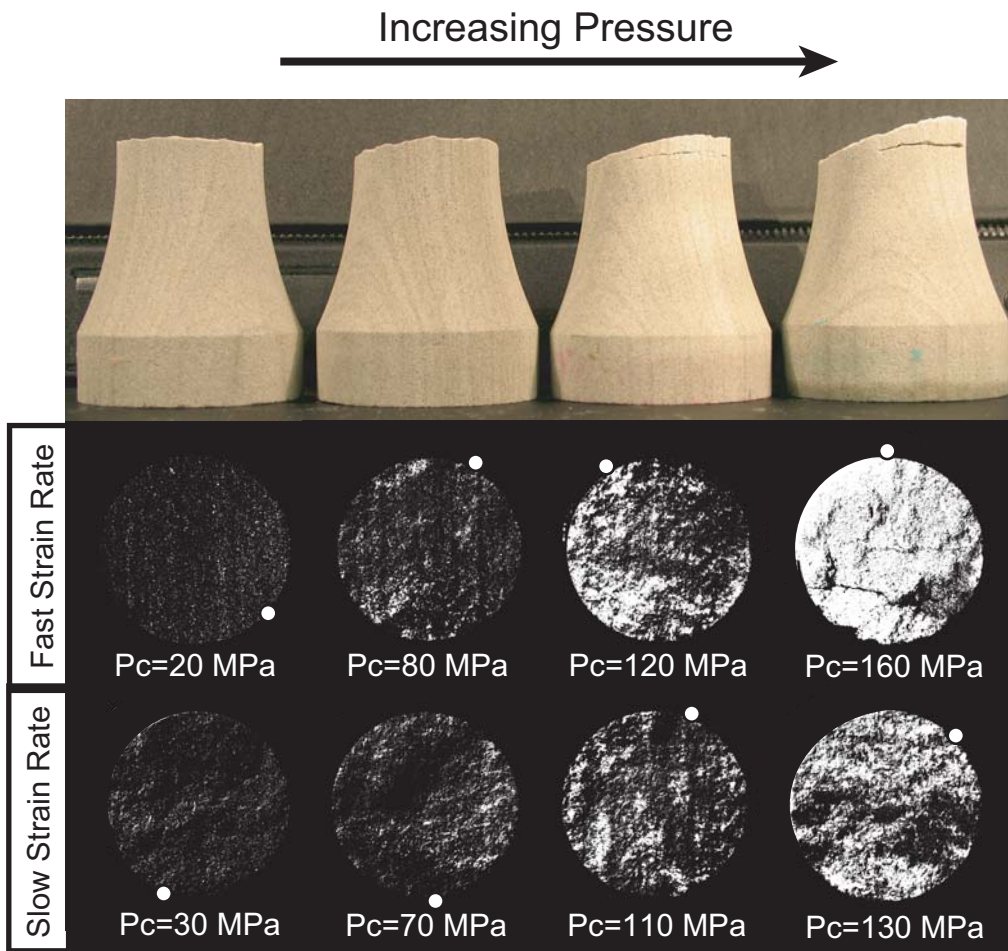
Figure 10. Photographs that represent morphological characteristics of fracture surfaces. *Upper:* A profile of fracture surfaces from copper-jacketed samples run at a strain rate of 10^{-4} s^{-1} is shown. Secondary fractures are probably a result of the unloading path. *Lower:* Images of corresponding fracture surfaces, representative of fast (10^{-4} s^{-1}) and slow (10^{-5} s^{-1}) strain rates, are thresholded to the point where laminae are just indistinguishable. White patches are zones of crushed grains that are an inherent feature of the fracture surface. Extension fracture surfaces at 20 MPa and 30 MPa do not have any zones of comminution, therefore the thresholded images represent background white. Note the similarity of the amount of comminution between the fast and slow strain rates. Dip direction of fracture surfaces is indicated by a white circle on the fracture perimeter.

DISCUSSION

Fracture Classification

An extension fracture is the experimental equivalent to a joint observed in outcrop, which is a fracture that propagates in the plane of the maximum principal stress and opens in pure dilation [*Hancock*, 1986]. Fractures that form in pure opening mode in porous, granular materials do so by intergranular and transgranular fracture [*Pollard and Aydin*, 1988]. By these criteria, extension fracture in Berea Sandstone occurs at confining pressures less than 50 MPa. Minimal inelastic strain occurs prior to formation of the macroscopic fracture surface, which is tan and granular in texture and is oriented approximately parallel to the maximum principal stress. Mechanical data indicates greater differential stresses and more tensile axial stresses are required to form extension fracture with an increase in mean stress.

Traditionally, fractures inclined 30° to the maximum principal stress with displacement in the plane of the fracture are defined as shear fractures [*Hancock,* 1986]. Formed in triaxial extension, shear fracture in Berea Sandstone is characterized by a totally white, comminuted fracture surface oriented approximately 15° to σ_1. Both the mechanical data and surface morphology indicate a gradual transition exists between extension and shear fracture, between 50 MPa $< Pc <$ 160 MPa. With increasing pressure, greater amounts of inelastic strain occur earlier in the strain history, fracture angles escalate, and greater amounts of white comminution develop on the fracture surface. These observations are similar to reports of fracture characteristics with increasing pressure by other experimentalists [*Ramsey and Chester*, 2004; *Bernabe and*

Brace, 1990; *Wong et al.,* 1997]. Failure strengths of the extension to shear fracture transition follow Coulomb behavior. There is no distinct change in mechanical behavior or fracture characteristics across the extension to shear fracture transition, indicating that there is no distinct difference in the failure mechanisms between mixed and compressive stress states or at the change in the sign of the normal stress across the fracture surface.

Failure Criteria and σ_2 Dependence

Triaxial extension data are compared to results of triaxial compression tests conducted on the same Berea Sandstone by other experimentalists in the John Handin Rock Deformation Laboratory (Table 3) in σ_1 and σ_3 stress space (Figure 11). A Coulomb relation (2) describes failure data for both triaxial extension and compression at $\sigma_1 < 210$ MPa, where $a = 94.7$ MPa and $b = 5.8$ (Figure 11). This Coulomb relationship is similar to that of triaxial extension data ($a = 98.7$ MPa, $b = 6.4$), although it overpredicts the failure strength of triaxial compression data at high pressure ($\sigma_1 > 210$ MPa) (Figure 11).

For $\sigma_1 > 50$ MPa, a parabolic envelope best approximates failure in Berea Sandstone in maximum and minimum principal stress space (Figure 11). The parabolic Mohr envelope is expressed as

$$\sigma_1 = a + b\,\sigma_3 + c\,\sigma_3{}^2 \qquad (4),$$

where $a = 97.0$ MPa, $b = 4.8$, and $c = -0.01$. The intercepts (a = 94.7 MPa, 98.7 MPa, 97.0 MPa) of the envelopes approximate $Co = 97$ MPa, which is greater than the observed uniaxial compressive strength, $Co = 79$ MPa [*Teufel and Clark*, 1984; *Krech et al.*, 1974].

TABLE 3. Peak stress values of triaxial compression tests on Berea Sandstone[1]

Experiment	Operator	σ_1 (MPa)	σ_3 = Pc (MPa)
[2]*Strain rate = 10^{-4}*			
4587	Ramsey	86	1
4583	Cubuk	79	5
4293	McLain	209	20
4531	Cubuk	256	40
4297	McLain	305	50
4292	McLain	428	100
4309	McLain	500	150
4311	Kuhle	523	170
[3]*Strain rate = 10^{-5}*			
[4] LC	Wong et al.	90.5	5
LC	Wong et al.	112	10
LC	Wong et al.	141	15
LC	Wong et al.	217	40
[5] CF	Wong et al.	370	160
CF	Wong et al.	445	250

[1] Room temperature, 24° C

[2] [*Texas A&M University*, 1998-2002]

[3] [*Wong et al.*, 1997]

[4] Localized shear; effective pressure

[5] Compactive cataclastic flow; effective pressure; σ_1 = onset of accelerated porosity reduction
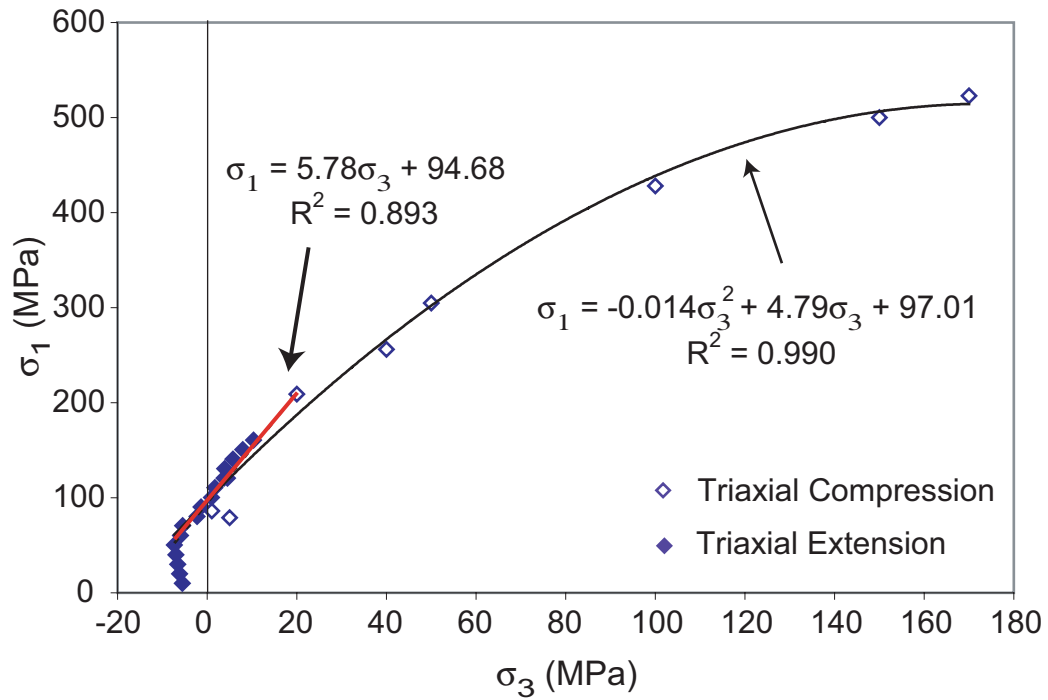
Figure 11. Triaxial extension and compression relationship: no σ_2 dependence. A Coulomb fit (red line) represents maximum principal stresses less than 210 MPa, and a parabolic fit considers all data except extension fracture. Triaxial compression data are from experimentalists at Texas A&M University, listed in Table 3.

The tensile strength (*To*) of Berea is represented by extending the failure envelope to be normal to the minimum principal stress axis, at $\sigma_3 = -7.3$ MPa. However, the trend of the failure envelope for extension fracture (*Pc* < 50 MPa) exhibits negative strength dependence with pressure, such that multiple values of maximum principal stress are possible for a given minimum principal stress (Figure 7). The 2.3 MPa decrease in axial stress with pressure for extension fracture in Berea Sandstone is greater than the ±0.3 MPa variability of direct pull tests [*Teufel and Clark*, 1984; *Hardy*, 1972], experimental variability of ±0.5 MPa, and the reproducibility experiment at 10 MPa (±0.7 MPa), and is not consistent with the assumption that the tensile strength is constant with an increase in pressure.

Polyaxial criteria are examined in order to identify a universal relationship that accounts for the affect of σ_2 in different experimental conditions. *Colmenares and Zoback* [2002] report that the Wiebols and Cook criterion is a good approximation of failure in true polyaxial conditions for highly σ_2–dependent rocks, such as sandstone and dolomite. The Modified Wiebols and Cook criterion [*Colmenares and Zoback*, 2002] is expressed as

$$J_2^{1/2} = A + BJ_1 + CJ_1^2 \tag{5},$$

where

$$J_2^{1/2} = \sqrt{\frac{1}{6}(\sigma_1 - \sigma_2)^2 + (\sigma_2 - \sigma_3)^2 + (\sigma_3 - \sigma_1)^2} \tag{6}$$

and

$$J_1 = \frac{\sigma_1 + \sigma_2 + \sigma_3}{3} \tag{7}.$$

In plotting the failure data for Berea Sandstone in triaxial compression and extension in J_1-$J_2^{1/2}$ stress space, $A = 4.033$ MPa, $B = 0.966$, and $C = -0.001$ (Figure 12). $J_2^{1/2}$ is identical in triaxial extension and compression, so the deviation of data points from the curve ($R^2 = 0.934$) is due to the σ_2-dependence of the mean stress. The undesirable fit of (5) indicates the inability of the Modified Wiebols and Cook criterion to predict failure in deviatoric and mean stress space for the end-member stress states of triaxial compression and extension, which agrees with experimental results of *Handin et al.* [1963] and *Heard* [1960].

The misfit of the extension and compression trends indicates that a reduction of the intermediate principal stress is required to compare data from different experimental conditions. The *Mogi* [1967] criterion weighs the effect of σ_2 with the coefficient β in the expression

$$\tau_{max} = \frac{\sigma_1 - \sigma_3}{2} = A\left(\frac{\sigma_1 + \beta\sigma_2 + \sigma_3}{2}\right)^{\alpha} \quad (8),$$

where a strong dependence on σ_2 corresponds to $\beta = 1$, and $\beta = 0$ when σ_2 is ignored. In combining experiments at low mean stress ($\sigma_m < 120$ MPa) from triaxial compression tests of other experimentalists on the same rock and by *Wong et al.* [1997] (Table 3), the best linear fit ($R^2 = 0.983$) between triaxial extension and compression data corresponds to $\beta = 0.18$. For experiments conducted in the John Handin Rock Deformation Laboratory, the power-law relationship in (8) that fits both triaxial extension and compression data ($R^2 = 0.993$) has $A = 2.92$, $\beta = 0.18$, and $\alpha = 0.70$ (Figure 13).
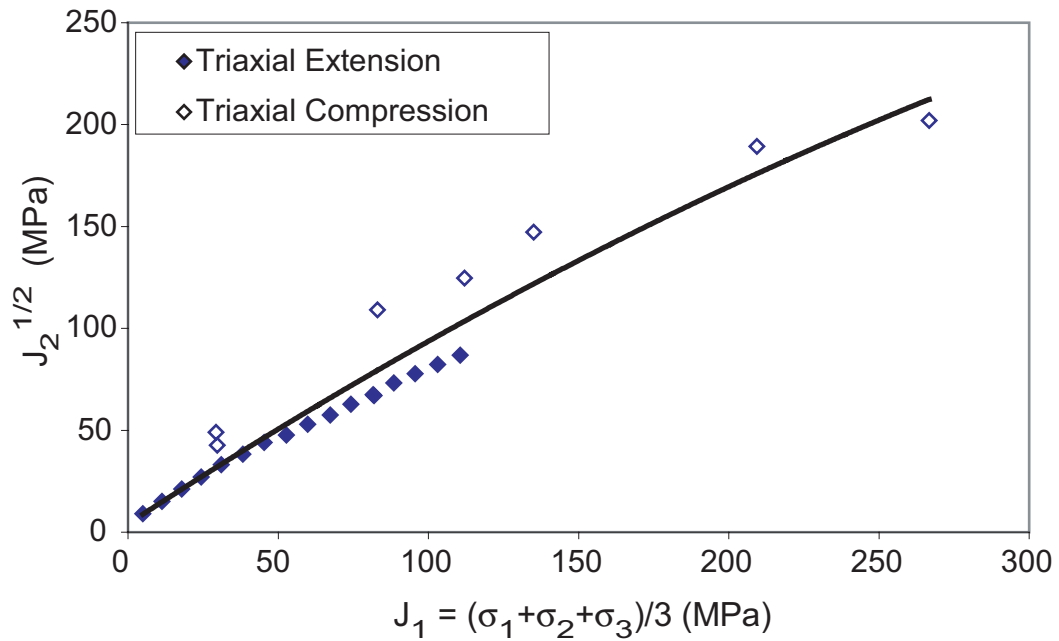
Figure 12. Polyaxial criterion for Berea Sandstone: Modified Wiebols and Cook criterion. The Modified Wiebols and Cook criterion [*Colmenares and Zoback*, 2002] poorly fits the triaxial extension and compression data. Triaxial compression data are from other experimentalists at Texas A&M University, listed in Table 3.
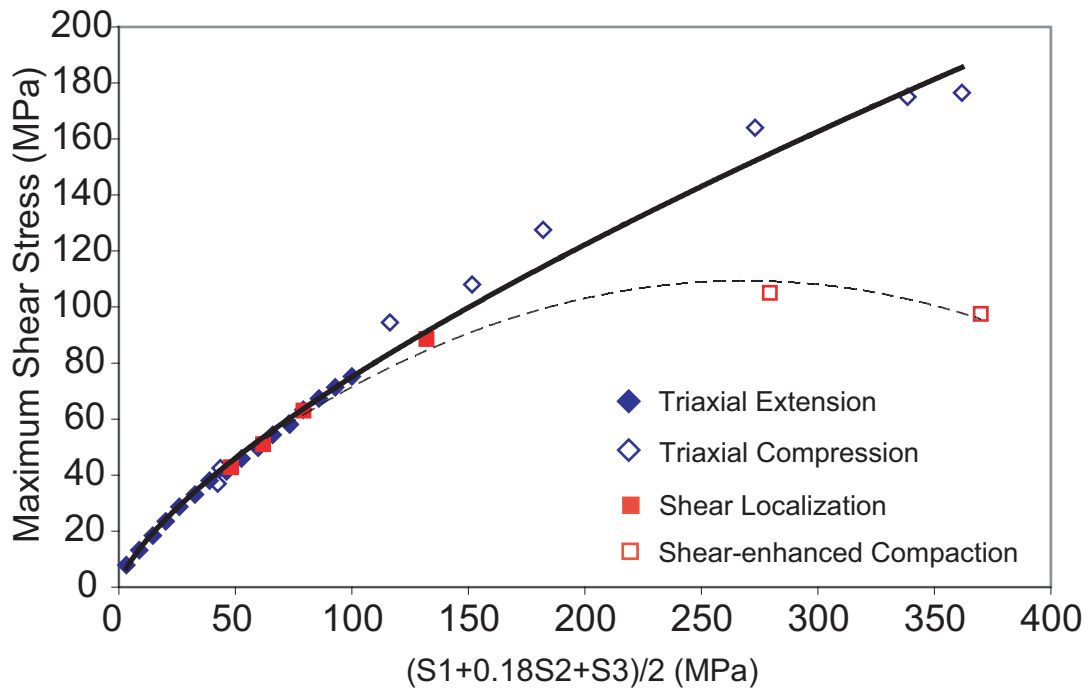
Figure 13. Polyaxial criterion for Berea Sandstone: Mogi criterion. Triaxial extension and compression data are related using the *Mogi* [1967] criterion. Triaxial compression data are from other experimentalists at Texas A&M University, and the red squares that represent shear localization and shear-enhanced compaction are from triaxial compression experiments on Berea Sandstone by *Wong et al.* [1997], listed in Table 3. The dashed curve approximates the onset of shear-enhanced compaction as determined by *Wong et al.* [1997].

The data points obtained by *Wong et al.* [1997] that represent the onset of shear-enhanced compaction in Berea Sandstone (Figure 13, Table 3) are determined from the point at which the effective mean stress deviates from the hydrostat due to an accelerated decrease in porosity relative to the hydrostat. In other porous rocks, the point of shear-enhanced compaction occurs at lower differential stress with increasing mean stress, resulting in an elliptical yield envelope [*Wong et al.,* 1997; *Zhu et al.*, 1997] (Figure 1). The onset of shear-enhanced compaction deviates from the peak stress values of triaxial compression data at corresponding mean stress (Figure 13). Thus, the point of shear-enhanced compaction may follow a separate yield envelope that predicts conditions of compactive cataclastic flow at high mean stress, and becomes less significant with decreasing mean stress.

Fracture Orientation Predictability

The Coulomb relationship is commonly used to predict fracture orientation in structural geology and rock mechanics, and has been successful at predicting the orientation of shear fractures formed in triaxial compression [*Handin et al.*, 1963; *Heard,* 1960]. Fracture angles formed in triaxial extension are compared with angles predicted by a Coulomb analysis of strength data from (2) (Figure 9). The linear Coulomb envelope results in predicted fracture angles of approximately 22° that do not change with pressure (Figure 9). Because observed fracture angles increase from 2° to 15° of σ_1 with pressure, the Coulomb analysis overpredicts fracture angles by 7° to 20°. Therefore, the Coulomb criterion is effective at estimating fracture angles in triaxial

compression, but is unsuccessful at predicting fracture orientation in triaxial extension at low mean stress.

Yielding and Fracture Development

Cumulative acoustic emissions between the hit point and the onset of the stress drop are compared to the amount of inelastic strain prior to macroscopic fracture (Figure 14). Acoustic emission counts increase with pressure, which corresponds to greater amounts of inelastic strain prior to macroscopic fracture. The trend of increasing acoustic emissions escalates under compressive stress states ($Pc > 100$ MPa), which relates to the significant increase of inelastic strain at $Pc > 100$ MPa (Figure 14).

The point in the strain history at which the onset of inelastic strain measured relative to a nonlinear elastic reference occurs is compared to changes in acoustic emission activity throughout each experiment (Figure 15). Both the averaged and unaveraged acoustic emission rates of 1 count/sec are shown to indicate the sensitivity of the averaging function to early, isolated acoustic emission events. The averaged and unaveraged rates of 1 count/sec at $Pc = 130$ MPa are separated by a 54% difference in strain, which is representative of the gradual onset of acoustic emissions for this experiment. Acoustic emissions initiate at 100% of total strain at $Pc = 10$ MPa and occur at earlier points in the strain history with increasing pressure, to 43% of total strain at $Pc = 130$ MPa (Figure 15). The percents of total strain at which AE initiate at a maximum principal stress of 10 MPa and 130 MPa are comparable to results of previous studies of mode I fracture in granite and micritic dolostone (at 100% strain) [*Glaser and*
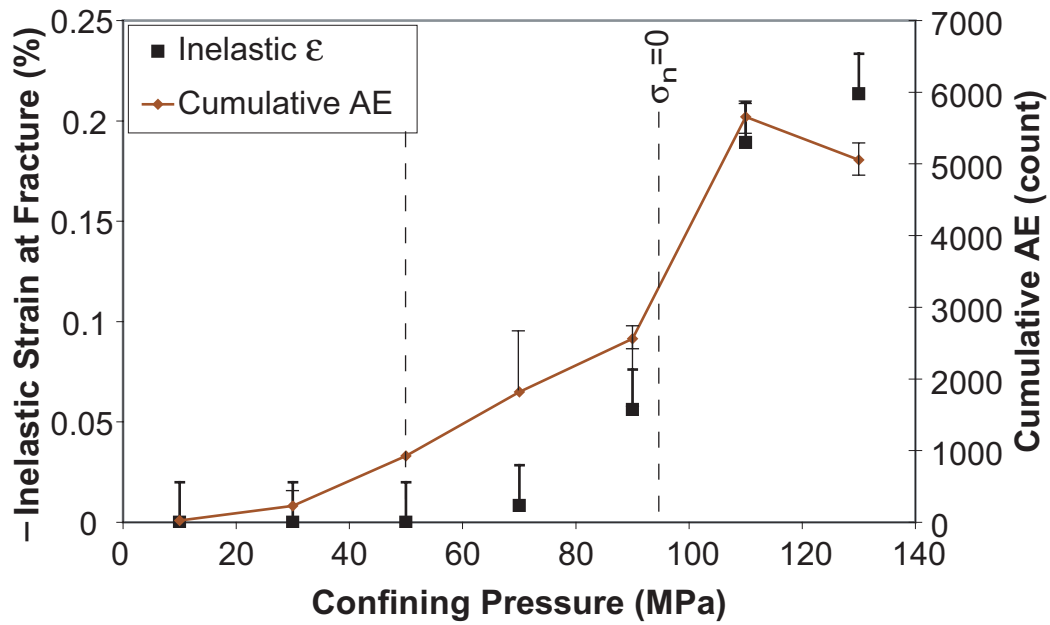
Figure 14. Relationship between cumulative AE and the amount of inelastic strain at fracture. Cumulative acoustic emissions are counted up to macroscopic fracture formation for copper-jacketed experiments run at a strain rate of 10^{-5} s^{-1}. The error bars represent difficulty in picking the initiation of stress drop and the 3% error of event counting. The percent of inelastic strain prior to macroscopic fracture formation is measured with respect to a nonlinear elastic reference curve.
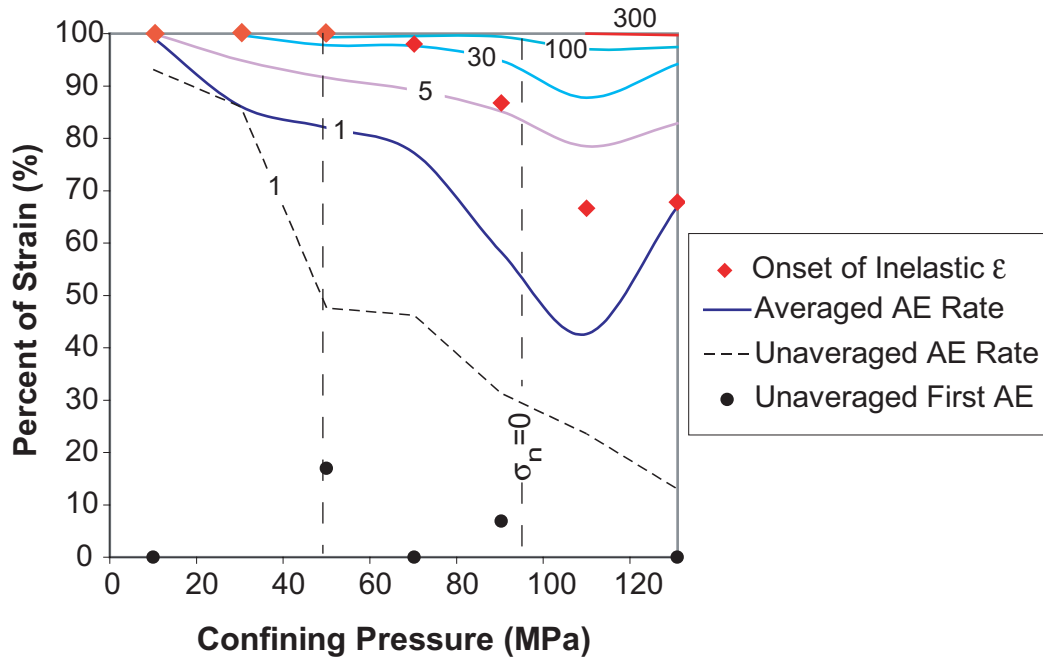
Figure 15. AE rate and inelastic strain changes with respect to percent axial strain and confining pressure. The data is from copper-jacketed samples run at a strain rate of 10^{-5} s^{-1}, and the onset of inelastic strain is measured with respect to a nonlinear elastic reference curve. Contour values are in units of counts/sec. The smoothed lines are rates averaged over 10 data points, and the unsmoothed, dashed line and circles represent the unaveraged data. The first occurrence of AE (solid circles) represents hit point acoustic emissions and isolated events early in the strain history. The deviation between the averaged and unaveraged 1 count/sec contours indicates the sensitivity of the averaging function to early acoustic emission events, whereas averaged and unaveraged contours of higher rates generally coincide.

Figure 16. Relationship between the peak stress, stresses corresponding to AE rate changes, and the Griffith criterion. Data is from copper-jacketed samples run at a strain rate of 10^{-5} s^{-1}. AE contour values are expressed in units of counts/sec. The Griffith criterion is calculated from latex-jacketed failure data, with To = 7.3 MPa.
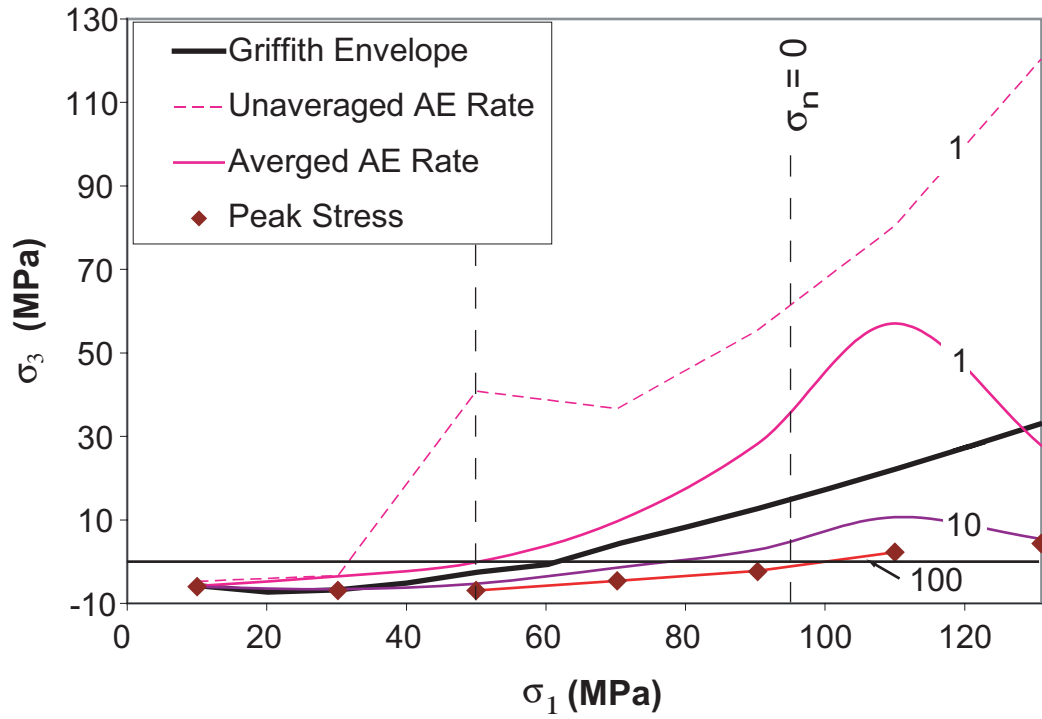
Nelson, 1992] and of shear fracture in porous sandstone (at 30% to 50% strain) [*Lockner et al.*, 1992; *Wong et al.*, 1997], respectively.

The onset of inelastic strain determined from a nonlinear elastic reference occurs at macroscopic fracture formation (= 100% of total strain) for *Pc* < 50 MPa, and begins at earlier points in the strain history with *Pc* > 50 MPa, to 67% of total strain at *Pc* = 130 MPa. The trend of the percent strain at which inelastic yielding initiates with pressure at *Pc* > 50 MPa has a similar inclination to the strain-*Pc* contour of the 1 count/sec averaged AE rate (Figure 15). In summary, inelastic deformation increases with pressure, occurs at earlier points in the strain history, and is related to energy associated with AE released through microcracking and frictional slip.

Changes in the rate of acoustic emissions are related to Griffith theory, which represents the initiation of fracture development (Figure 16). The Griffith criterion is written as

$$\sigma_3 = -4\sqrt{T_O{}^2 - T_O\sigma_1} + 4T_O - \sigma_1 \qquad (9),$$

where *To* is the tensile strength of the material [*Jaeger*, 1969]. The tensile strength used in (9) for this analysis is 7.3 MPa, which the maximum tensile strength of Berea (Figure 7).

The Griffith criterion is compared to changes in inelastic deformation (represented by AE rate changes and peak stress) in maximum and minimum principal stress space (Figure 16). Macroscopic extension fracture (*Pc* < 50 MPa) occurs at stresses where the Griffith criterion approximates the onset of fracture, whereas σ_3 at peak differential stress is underestimated by the Griffith envelope at *Pc* > 50 MPa.

However, the character of AE rates contoured in σ_3 versus σ_1 space follows the Griffith trend, and the averaged AE rate of 1 count/sec correlates most strongly to the stresses at which Griffith theory predicts the onset of fracture (Figure 16). Therefore, the Griffith criterion successfully predicts the onset of inelastic strain related to acoustic activity, which occurs earlier in the stress history with pressure.

Lithology Comparison

The rock type, specimen assembly and procedure used in this study are designed to be comparable to a previous study of hybrid fracture in Carrara Marble, a low porosity, polycrystalline calcite rock [*Ramsey and Chester*, 2004]. The sandstone and marble are similar in compressive and tensile strength and grain size, but are different in composition and porosity (Table 1). The quartz in Berea fails by brittle microfracture, whereas the polycrystalline calcite of Carrara deforms by crystal plasticity in addition to microfracture. Carrara Marble is nearly nonporous while Berea Sandstone has a high porosity, where the granular texture complicates local stress distributions and Hertzian contacts control deformation.

The surface morphology of fractures in both lithologies is similar. Carrara Marble displays "highly reflective intergranular cleavage planes" on extension fracture surfaces, and shear fractures exhibit "comminuted, powdery-white material with short lineations" [*Ramsey and Chester*, 2004]. Similar to Berea Sandstone, the fracture surfaces in Carrara Marble gradually incorporate more morphological attributes of shear fracture and less evidence of extension fracture with increasing differential stress [*Ramsey and Chester*, 2004].
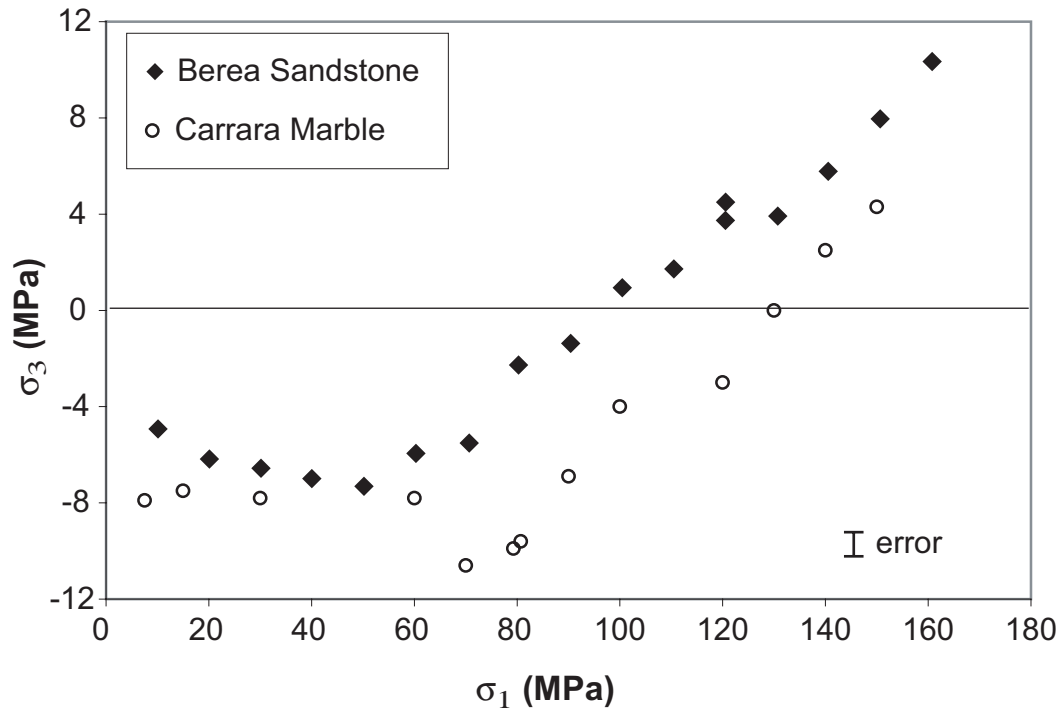
Figure 17. Comparison of failure data for Berea Sandstone and Carrara Marble. Results of Carrara Marble are from a previous study by *Ramsey and Chester* [2004]. Data from both studies is from latex-jacketed samples extended at the same rate.

Mechanical data that represents the extension to shear fracture transition in sandstone and marble is remarkably comparable. In both lithologies, Young's modulus increases with pressure, although the apparent change may be due to a strengthening of the apparatus with pressure. A change in strength dependence with mean stress occurs at the highest pressure at which macroscopic extension fracture forms in both Berea and Carrara (Figure 17). This change in slope likely reflects the increase in mean stress that suppresses the propagation of extension fractures, and the interaction between closely-spaced stepped cracks. In both lithologies, failure strengths of the extension to shear fracture transition exhibit Coulomb behavior (Figure 17). The increase in fracture angle with pressure is nearly identical for sandstone and marble (Figure 9).

The dependence of tensile strength on pressure varies with lithology, which identifies the effects of grain-scale deformation mechanism differences of sandstone and marble. Tensile strengths of extension fracture in marble are independent of pressure [*Ramsey and Chester*, 2004], contrary to the increase in tensile strength with pressure observed in sandstone (Figure 17). The increase in the tensile strength of Berea Sandstone with pressure could be due to hydrostatic, elastic reduction of pore space in the starting material, which is enhanced in granular materials deformed in triaxial extension experiments that begin at a hydrostatic, maximum stress state before reducing the axial stress. The reduction of pore space with increasing starting pressure increases the mean area of grain contacts and the normal stress across grain contacts, and is not possible for low-porosity Carrara Marble. The increase in the mean contact area of

grains could enhance the effect of σ_2 at low pressure, and greater alleviation of normal stress is required to form intergranular fracture with increasing pressure.

Geological Conditions

The state of stress with depth can be constrained using experimental data of rock strength. The frictional strength of fractured rock increases linearly with pressure independent of lithology [*Byerlee*, 1978], and adequately predicts measured values of horizontal lithospheric stress in the Earth to 4 km depth assuming hydrostatic pore pressure [*Brace and Kohlstedt*, 1980]. My results on brittle failure at low mean stress may be used to predict the stress conditions for fracture of intact rock at depth. To first-order, the strength of rock follows a linear dependence on pressure, in agreement with high-pressure experimentation by *Bernabe and Brace* [1990] and *Handin et al.* [1963]. In the following, I estimate the conditions for extension and shear fracture in both extensional and compressional geologic settings.

Following *Anderson* [1951] and subsequent workers, an extensional environment is characterized by vertical maximum principal stress and horizontal minimum principal stress, where a tensile horizontal stress may originate from tectonic loading and be enhanced by elevated pore pressure. Assuming a lithostatic gradient of 26 MPa/km [*Brace and Kohlstedt,* 1980] and a hydrostatic water column with interconnected voids, the effective (vertical) maximum principal stress gradient is approximately 16 MPa/km. If tectonic loading reduces the horizontal stress to failure, then the experimental results for porous sandstone, similar to Berea Sandstone, should exhibit a transition from extension to shear fracture at a depth of 3 to 6 km (Figure 7).

A compressional setting is characterized by a horizontal maximum principal stress and vertical minimum principal stress. In this setting, the vertical stress cannot become tensile unless overpressure occurs as a result of impermeable fault barriers or lithology traps. To propagate an extension fracture in an overpressured setting, the fluid pressure must be equivalent to the sum of the minimum principal stress and the tensile strength of the rock [*Sibson,* 1996]. Under these conditions, the fracture transition should occur at depths where the horizontal stress is between 50 to 100 MPa. Such fluid pressures are much less likely to occur and therefore the fracture transition is more likely observed in extensional environments.

Mixed tensile and compressive stress states can also be achieved locally in various environments. For instance, at the hinge of folded rock, the stress state changes from compressive on the inner bend of the fold, across a neutral fiber where the state of stress is homogenous, to a tensile stress state at the outer bend of the flexure. Shear fractures form in the compressive realm, proximal to the inner portion of the hinge, and joints develop in the tensile, outer bend of the hinge axis [*Ramsey*, 1967]. Fractures that exhibit features of both extension and shear occur near the neutral fiber, where mixed tensile and compressive stress conditions interact.

For petroleum and gas reservoirs, it is important to distinguish where fractures with dilational properties (extension and hybrid fracture) form, and where fractures that may have impermeable or directional properties (shear fracture) develop. Additionally, the orientation of macroscopic joint and fault networks and the development of fracture meshes are important to reservoir permeability. Joint networks result in a highly

directional reservoir permeability [*Sibson*, 1996], occurring at depths less than 3 km in

an extensional setting with hydrostatic fluid pressure. The significance of reservoir

compartmentalization increases with development of fault networks at depths greater

than 10 km in extensional settings. At intermediate depths, fractures inclined from 4 to

15° of the maximum principal stress develop mesh networks with a dilational

component. The result is a mesh network with high permeability in the σ_2 direction

[*Sibson*, 1996] and less compartmentalization than a fault network.

CONCLUSIONS

Acoustic emissions, force, displacement, and confining pressure were monitored in triaxial extension experiments on notch-cut samples of Berea Sandstone, and permit a detailed analysis of the extension to shear fracture transition in porous granular rock.

Extension fracture in Berea Sandstone forms at confining pressures less than 50 MPa. Minimal inelastic strain occurs prior to formation of the macroscopic extension fracture surface, which is tan and granular in texture and is oriented approximately parallel to the maximum principal stress. More tensile axial stresses are required to form extension fractures with increasing pressure. This increase in tensile strength with pressure is not observed in low porosity, polycrystalline Carrara Marble, which suggests that porosity and Hertzian contacts strongly affect extension fracture formation in triaxial extension. Shear fracture is characterized by a totally white, comminuted fracture surface oriented approximately 15° to σ_1.

The extension to shear fracture transition (50 MPa $< Pc <$ 160 MPa) is expressed by gradual changes in mechanical behavior and morphological characteristics of fracture surfaces, similar to those observed in polycrystalline Carrara Marble.

1. Failure strengths follow Coulomb behavior, and when combined with triaxial compression data, may be described using a power law *Mogi* [1967] relationship that includes a dependence on σ_2.

2. Fracture angle escalates from 2° to 15° with increasing pressure, and cannot be predicted by a Coulomb-Mohr analysis.

3. The fracture surface morphology includes features of both extension and shear fracture. Patches of white, comminuted sandstone on the fracture surface increase in size and total area with increasing pressure. The granular, tan morphology becomes less prominent with pressure, and it forms under both mixed and compressive stress states.

Inelastic deformation prior to macroscopic fracture formation is expressed as acoustic emissions; more acoustic emissions occur prior to macroscopic failure with increasing pressure. At low pressure ($Pc = 10$ MPa), acoustic emissions initiate at peak stress of fracture formation. With an increase in pressure, AE initiate at earlier points in the strain history. At $Pc = 130$ MPa, the onset of acoustic emissions occurs at approximately 2/5 of total strain. The Griffith criterion successfully predicts the onset of fracture formation relative to the initiation of acoustic activity, using the experimentally determined tensile strength of 7.3 MPa.

REFERENCES

Anderson, E.M., *The Dynamics of Faulting and Dyke Formation with Application to Britain, 2ⁿᵈ Edition*, 206 pp., Oliver and Boyd, Edinburgh, 1951

Antonellini, M.A., and A. Aydin, Effect of faulting on fluid flow in porous sandstones: Geometry and spatial distribution, *AAPG Bulletin*, *79,* 642-671, 1995.

Antonellini, M.A., and A. Aydin, Effect of faulting on fluid flow in porous sandstones: Petrophysical properties, *AAPG Bulletin*, *78,* 355-377, 1994.

Antonellini, M.A., Aydin, A., and D.D. Pollard, Microstructure of deformation bands in porous sandstones at Arches National Park, Moab, Utah, *Journal of Structural Geology*, *16*, 941-959, 1994.

Bernabe, Y., and W.F. Brace, Deformation and fracture of Berea Sandstone, in *The Brittle-Ductile Transition in Rocks, The Heard Volume, Geophysical Monograph Series, Vol. 56,* edited by A.G. Duba, pp. 91-102, American Geophysical Union, Washington DC, 1990.

Bernard, X.D., Eichhubl, P., and A. Aydin, Dilation bands: A new form of localized failure in granular media, *Geophysical Research Letters*, *29*, 29-1 – 29-4, 2002.

Besuelle, P., Compacting and dilating shear bands in porous rock: Theoretical and experimental conditions, *Journal of Geophysical Research*, *106*, 13,435-13,442, 2001.

Besuelle, P., Desrues, J., and S. Raynaud, Experimental characterization of the localization phenomenon inside a Vosges sandstone in a triaxial cell, *International Journal of Rock Mechanics and Mining Sciences, 37*, 1223-1237, 2000.

Brace, W.F., Brittle fracture of rocks, in *State of Stress in the Earth's Crust,* edited by W.R. Judd, pp. 111-180, American Elsevier, New York, 1964.

Brace, W.F., and D.L. Kohlstedt, Limits on lithospheric stress imposed by laboratory experiments, *Journal of Geophysical Research, 85,* 6248-6252, 1980.

Brzesowsky, R., Micromechanics of sand grain failure and sand compaction, Ph.D. Dissertation, 180 pp., University of Utrecht, The Netherlands, 1995.

Byerlee, J.D., Friction of rocks, *Pure Applied Geophysics, 116,* 615-626, 1978.

Challa, V. and K.A. Issen, Conditions for compaction band formation in porous rock using a two-yield surface model, *Journal of Engineering Mechanics, 130*, 1089-1097, 2004.

Colmenares, L.B., and M.D. Zoback, A statistical evaluation of intact rock failure criteria constrained by polyaxial test data for five different rocks, *International Journal of Rock Mechanics and Mining Sciences, 39*, 695-729, 2002.

Cruden, D.M., Single-increment creep experiments on rock under uniaxial compression, *International Journal of Rock Mechanics and Mining Sciences, 8,* 127-142, 1971.

Gallagher, J.J., Friedman, M., Handin, J., and G.M. Sowers, Experimental studies relating to microfracture in sandstone, *Tectonophysics, 21,* 203-247, 1974.

Glaser, S.D., and P.P. Nelson, Acoustic emissions produced by discrete fracture in rock: Part 2- Kinematics of crack growth during controlled mode I and mode II loading of rock, *International Journal of Rock Mechanics and Mining Sciences and Geomechanical Abstracts, 29,* 253-265, 1992.

Hancock, P.L., Joint spectra, in *Geology in the Real World – the Kingsley Dunham Volume*, edited by Nichol, I., Nesbitt, R.W., pp. 155-164, Institution of Mining and Metallurgy, London, 1986.

Handin, J., Hager, R.V., Friedman, M., and J.N. Feather, Experimental deformation of sedimentary rocks under confining pressure: Pore pressure tests, *AAPG Bulletin, 47*, 717-755, 1963.

Hardy, H.R., Hoop-stress loading- a new method of determining the tensile strength of rock, *Society of Petroleum Engineers Journal, 253*, 246-252, 1972.

Hart, D.J, and H.F. Wang, Laboratory measurements of a complete set of poroelastic moduli for Berea sandstone and Indiana limestone, *Journal of Geophysical Research, 100,* 17,741-17,751, 1995.

Heard, H.C., Transition from brittle fracture to ductile flow in Solenhofen limestone as a function of temperature, confining pressure, and interstitial fluid pressure, Chapter 7, in *Rock Deformation-A Symposium: Geological Society of America Memoir*, edited by Griggs, D.T., pp. 193-226, Boulder, CO, 1960.

Hillard, J.E., and L.R. Lawson, *Stereology and Stochastic Geometry*, 488 pp., Kluwer Academic Publishers, Dordrecht, The Netherlands, 2003.

Issen, K.A. and V. Challa, Conditions for dilation band formation in granular materials, *16th ASCE Engineering Mechanics Conference*, University of Washington, Seattle, 1-4, 2003.

Jaeger, J.C., *Elasticity, Fracture and Flow with Engineering and Geological Applications*, 268 pp., Chapman and Hall, New York, 1969.

Johnson, B., Friedman, M., Hopkins, T.W., and S.J. Bauer, Strength and microfracturing of Westerly Granite extended wet and dry at temperatures to 800°C and pressures to 200 MPa, in *Rock Mechanics: Proceedings of the 28th U.S. Symposium,* edited by I.W. Farmer, pp. 399-412, Rotterdam, The Netherlands, 1987.

Krech, W.W., Henderson, F.A., and K.E. Hjelmstad, A standard rock suite for rapid excavation research, *International Journal of Rock Mechanics and Mining Science and Geomechanics Abstracts, 11*, 198, 1974.

Lockner, D.A., Byerlee, J.D., Kuksenko, V., Ponomarev, A., and A. Sidorin, Observations of quasistatic fault growth from acoustic emissions, in *Fault Mechanics and Transport Properties of Rocks,* edited by B. Evans and T-F. Wong, pp. 3-32, Academic Press, London, 1992.

Mardon, D., Kronenberg, A.K., Handin, J., Friedman, M., and J.E. Russell, Mechanisms of fracture propagation in experimentally extended Sioux quartzite*, Tectonophysics, 182*, 259-278, 1990.

Menendez, B., Zhu, W., and T-F Wong, Micromechanics of brittle faulting and cataclastic flow in Berea sandstone, *Journal of Structural Geology, 18*, 1-16, 1996.

Mogi, K., Effect of the intermediate principal stress on rock failure, *Journal of Geophysical Research, 72,* 5117-5131, 1967.

Mollema, P.N. and M.A. Antonellini, Compaction bands: A structural analog for anti-mode I cracks in aeolian sandstone, *Tectonophysics, 267*, 209-228, 1996.

Pollard, D.D., and A. Aydin, Progress in understanding jointing in the last century, *Geological Society of America Bulletin, 100,* 1181-1204, 1988.

Ramsey, J., and F. Chester, Hybrid fracture and the transition from extension fracture to shear fracture, *Nature, 428,* 63-66, 2004.

Ramsey, J.G., *Folding and Fracturing of Rocks*, 560 pp., McGraw-Hill Book Company, New York, 1967.

Rodriguez, E., A microstructural study of the extension-to-shear-fracture transition in Carrara Marble, M.S. Thesis, 61 pp., Texas A&M University, 2005.

Schock, R.N., and H. Louis, Strain behavior of a granite and a greywacke sandstone in tension, *Journal of Geophysical Research, 87,* 7817-7823, 1982.

Sibson, R.H., Structural permeability of fluid-driven fault-fracture meshes, *Journal of Structural Geology, 18*, 1031-1042, 1996.

Teufel, L.W., and J.A. Clark, Hydraulic fracture propagation in layered rock: Experimental studies of fracture containment, *Society of Petroleum Engineers Journal, 24*, 19-32, 1984.

Texas A&M University, John Handin Rock Deformation Laboratory, Large Specimen Rig Triaxial Compression Experiments, Department of Geology and Geophysics, College Station, TX, 1998-2002.

Wong, T.F., David, C., and W. Zhu, The transition from brittle faulting to cataclastic flow in porous sandstones: Mechanical deformation, *Journal of Geophysical Research, B, Solid Earth and Planets, 102,* 3009-3025, 1997.

Zhang, J., Wong, T-F., and D.M. Davis, Micromechanics of pressure-induced grain crushing in porous rocks, *Journal of Geophysical Research, 95,* 341-352, 1990.

Zhu, W., Montesi, L.G.J, and T-F. Wong, Shear-enhanced compaction and permeability reduction: Triaxial extension tests on porous sandstone, *Mechanics of Materials, 25,* 199-214, 1997.
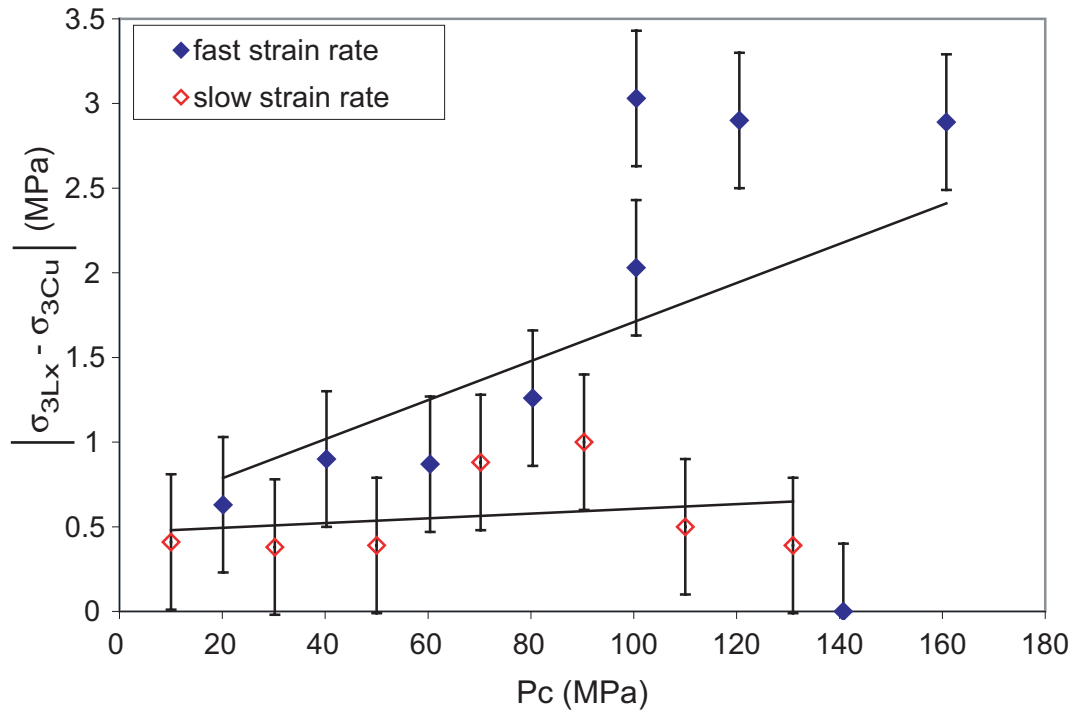
APPENDIX A

Figure A-1. Method used for obtaining the strength of the copper jacket. Error bars represent accuracy of experimentation. Absolute values are only significant to data from a slow strain rate, where the strength of the copper is sometimes greater than that of the latex due to the similarity in failure strength.

VITA

JENNIFER K. BOBICH

M.T. Halbouty Building • College Station, TX 77843
jkb152@hotmail.com

Education
Master of Science in Geology, August 2005
Texas A&M University, College Station, TX
Cumulative GPA: 3.87

Bachelor of Science in Geosciences, May 2002
Penn State University, University Park, PA
Cumulative GPA: 3.62

Research Experience

2004, Present	Exploration / Production Geologist
	3D Seismic Interpretation
	Shell Exploration and Production Company, New Orleans, LA
2003-2005	Research Assistant
	Experimental Rock Deformation
	Texas A&M University, College Station, TX
	Lab Technician
2000, 2001	Measurement of Thermal Conduction
	Penn State University, University Park, PA
1998, 1999	Quality Control of Developer Products
	Vertex Image Products, Inc., Yukon, PA
2000	Academic Intern
	Structural Geology Analyses
	University of Minnesota, Minneapolis, MN

Field Experience

	Field Geology Student and Assistant
2004	Guadalupe Mountains, TX; Carlsbad, NM
	ExxonMobil, Houston, TX
2003	Arches National Park, UT; Grand Canyon, AZ
	Texas A&M University, College Station, TX
2001	Ouachita Mountains, OK; Book Cliffs, UT; Elk Basin, WY
	Penn State University, University Park, PA